

Jet-cloud collisions in the jet of the Seyfert galaxy NGC 3079

E. Middelberg^{1*}, I. Agudo,^{2,3} A. L. Roy², and T. P. Krichbaum²

¹*Australia Telescope National Facility, PO Box 76, Epping NSW 1710, Australia*

²*Max-Planck-Institut für Radioastronomie, Auf dem Hügel 69, 53121 Bonn, Germany*

³*Instituto de Astrofísica de Andalucía, CSIC, Apartado 3004, 18080 Granada, Spain*

ABSTRACT

We report the results from a six-year, multi-epoch very long baseline interferometry monitoring of the Seyfert galaxy NGC 3079. We have observed NGC 3079 during eight epochs between 1999 and 2005 predominantly at 5 GHz, but covering the frequency range of 1.7 GHz to 22 GHz. Using our data and observations going back to 1985, we find that the separation of two of the three visible nuclear radio components underwent two decelerations. At the time of these decelerations, the flux density of one of the components increased by factors of five and two, respectively. We interpret these events as a radio jet component undergoing compression, possibly as a result of a collision with ISM material. This interpretation strongly supports the existence of jets surrounded by a clumpy medium of dense clouds within the first few parsecs from the central engine in NGC 3079. Moreover, based on recently published simulations of jet interactions with clumpy media, this scenario is able to explain the nature of two additional regions of ageing synchrotron material detected at the lower frequencies as by-products of such interactions, and also the origin of the kpc-scale super bubble observed in NGC 3079 as the result of the spread of the momentum of the jets impeded from propagating freely. The generalization of this scenario provides an explanation why jets in Seyfert galaxies are not able to propagate to scales of kpc as do jets in radio-loud AGN.

Key words: galaxies: active, galaxies: jets, galaxies: Seyfert, galaxies: individual: NGC 3079

1 INTRODUCTION

Active galactic nuclei (AGN) are conventionally divided into radio-loud and radio-quiet objects, depending on their ratio of radio-to-optical luminosity. Although radio-quiet objects such as Seyfert galaxies have luminosities of up to 1000 times less than radio-loud objects, they mostly exhibit high-brightness temperature (non-thermal) components (Middelberg et al. 2004), indicating that the radio emission is synchrotron emission. However, it is not clear why the generation of radio emission in Seyfert galaxies is different from that in radio-loud objects such as quasars and radio galaxies. In particular, Seyferts mostly do not exhibit long and confined jets as are typically observed in radio-loud objects. Only in few radio-quiet objects have jet-like features been observed, prominent examples are NGC 4258 (Miyoshi et al. 1995), NGC 4151 (Mundell et al. 2003), NGC 3079 (Irwin & Seaquist 1988; Trotter et al. 1998; Kondratko et al. 2005), and NGC 1068 (Roy et al. 1998),

NGC 3079 is a nearby (15.0 Mpc, de Vaucouleurs et al. 1991, $H_0 = 75 \text{ km s}^{-1} \text{ Mpc}^{-1}$, $1 \text{ mas yr}^{-1} = 0.24 c$) LINER (Heckman 1980) or Seyfert 2 (Sosa-Brito et al. 2001) galaxy in an edge-on, dusty spiral. In the radio, pilot VLBI observations by Irwin & Seaquist (1988) resolved the core into two strong components, *A* and *B*, separated by 20.2 mas. VLBI observations

carried out by Trotter et al. (1998), Sawada-Satoh et al. (2000), Kondratko et al. (2005) and Middelberg et al. (2005) revealed that the separation of *A* and *B* was increasing at a speed between $0.11 c$ and $0.16 c$ between 1985 and 2000. On the axis connecting *A* and *B*, indications of another component called *C* were already found by Irwin & Seaquist (1988). With very sensitive observations it has recently been possible to detect a structure that covers about half the projected distance of 2 pc between *A* and *B* (Kondratko et al. 2005), indicating a jet-like feature. NGC 3079 therefore appears to be a promising candidate source to investigate the nature of radio emission in Seyferts.

NGC 3079 also contains one of the brightest known extragalactic water masers ($\nu_{\text{rest}} = 22.23508 \text{ GHz}$), which has been subject to investigation for more than a decade (e.g., Haschick & Baan 1985; Haschick et al. 1990; Trotter et al. 1998; Kondratko et al. 2005). The distribution of the masers and their velocity dispersion indicate a thick molecular disk rotating around a massive object, presumably a black hole.

We have observed the radio emission in NGC 3079 with the VLBA at 5 GHz, 15 GHz, and 22 GHz, using phase referencing in most epochs, to monitor precisely its structural evolution. Single epoch images at 1.7 GHz and 2.3 GHz were obtained to probe a wider spectral range.

* E-mail: enno.middelberg@csiro.au

2 OBSERVATIONS

The data presented here were obtained with the VLBA over eight epochs between 1999 and 2005, partly supplemented by other telescopes. The sensitivity, (u, v) coverage, and resolution varied due to the wide range in frequency. Also, phase referencing was used in the later observations, but not in the 1999/2000 observations. A summary of the observations is presented in Table 1.

At 1.7 GHz and 2.3 GHz, NGC 3079 was observed during a single epoch only, on 22 September 2002, using phase referencing to the nearby calibrator 4C+55.17. The Effelsberg telescope was included in the 1.7 GHz observations only, to increase the resolution at this low frequency.

We have observed NGC 3079 at 5 GHz during eight epochs between November 1999 and August 2005 with the VLBA, in part supplemented by the Effelsberg telescope and a single VLA antenna. The observations carried out in 2002-2005 were phase-referenced to the nearby source 4C+55.17. We have also obtained a 5 GHz VLBI image from a 16-station global VLBI snapshot observation performed in 1994 (project GK011), but were only able to reliably measure the separation of A and B from this observation.

During three epochs in 1999-2000, we have observed NGC 3079 at 15 GHz with the VLBA, the Effelsberg telescope and a single VLA antenna. The observations yielded only few detections on some baselines shorter than $100 \text{ M}\lambda$ during the November 1999 and April 2000 epochs, but in November 2000, the source was detected on most baselines shorter than $120 \text{ M}\lambda$.

During the three epochs in 2004-2005, we observed the water maser emission in NGC 3079 at $\nu_{\text{rest}} = 22.23508 \text{ GHz}$ and the 22 GHz continuum emission. The frequency resolution was 31.25 kHz , corresponding to a velocity resolution of 0.42 km s^{-1} . The continuum emission was phase-referenced to the brightest maser feature.

2.1 Calibration

The data were calibrated using standard procedures implemented in the Astronomical Image Processing System, AIPS. The visibility amplitudes were calibrated using noise-adding radiometry and established antenna gains, and amplitude errors of the order of 5% arising from sampler threshold variations were corrected using the autocorrelation data. Phase rotation due to parallactic angle changes was corrected, and instrumental delays were calibrated using fringe-fitting on a short observation of a strong source. For phase calibration of the observations carried out in 1999-2000, we fringe-fitted the data using a point source model, with solution intervals of around 4 min, yielding detections on baselines up to $100 \text{ M}\lambda$ at both 5 GHz and 15 GHz. At 22 GHz, the phase calibration was carried out using six frequency channels with a total bandwidth of 187.5 kHz for self-calibration on the strongest water maser feature, at a velocity of 956 km s^{-1} . The maser was detected on most baselines, and the phase solutions were then applied to all frequency channels.

2.2 Earth orientation parameter errors and phase calibrator position changes

The observations in 2004 and 2005 were correlated using predicted rather than measured earth orientation parameters, a situation arising from a software upgrade at the VLBA correlator. Furthermore, the position of the phase calibrator 4C+55.17 used for phase referencing of the 5 GHz observations in the two 2005 epochs differed

from the position used in earlier epochs. This happened because calibrator positions in the program used to schedule VLBA observations, SCHED, were taken from a data base at the Array Operations Center at the time of observing, rather than from the schedule, and hence were subject to unforeseeable changes. However, the effects of both problems are predictable and precisely known, and were easily rectified.

We retrieved the final earth orientation parameters from the USNO solution at http://gemini.gsfc.nasa.gov/solve_save/usno_finals.erp and applied the corrections to the data using the AIPS task VLBAEOP. This process has been well tested and the residual phase errors after correction are of the order of $< 5^\circ$ at 5 GHz (Walker et al. 2005). The position of the calibrator in the 2002-2004 observations, 4C+55.17, was modified using the AIPS task CLCOR. The right ascension was decreased by 3.375 mas and the declination was decreased by 0.792 mas , to agree with the presumably more accurate position used in the 2005 observations, RA=09:57:38.184971, Dec=55:22:57.76924 (J2000).

2.3 Image analysis

The relative positions and flux densities of the 5 GHz and 15 GHz observations in 1994 and 1999-2000 were measured from self-calibrated images (because no phase referencing was carried out), tapered to a resolution of $3 \times 3 \text{ mas}^2$ as a compromise between (u, v) coverage and sensitivity. Absolute positions were not measured in these observations.

The absolute positions of the 5 GHz and 22 GHz observations in 2002-2005 were measured from purely phase-referenced images, with no self-calibration steps carried out, and tapered to $3 \times 3 \text{ mas}^2$. The flux densities at 5 GHz were measured from phase-referenced, self-calibrated, and tapered images, to remove residual phase errors and improve the signal-to-noise ratio. Flux densities at 22 GHz were measured from purely phase-referenced images because self-calibration turned out to be marginal. In self-calibration, the resulting flux densities of components A and B were found to vary by as much as a factor of three when the calibration strategy was changed only very little and our models did not reliably converge. We therefore consider the 22 GHz flux densities to be very unreliable and do not use them in our analysis.

We have measured the positions of components A , B , and E and their peak flux densities by fitting a paraboloid to a square of three by three pixels, using the location of the brightest pixel as a starting point. Exploring five images from a reasonable imaging parameter space revealed a position uncertainty of 0.15 mas (1σ) for the 5 GHz and 15 GHz images, and of 0.1 mas for the 22 GHz images. Hence separations, which include two position measurements, have errors of $\sqrt{2}$ times the position errors. The errors of our 1994 observations are larger because of the very sparse (u, v) coverage.

Integrated flux densities were measured by integrating over the source region. We have estimated the flux-density errors as follows: peak flux densities have a 5% (10%) scaling error at frequencies at and below 5 GHz (15 GHz) plus the image rms added in quadrature. Integrated flux densities have the same scaling errors, plus the image rms in quadrature, plus an error arising from the integration over the source region, which was derived experimentally, added in quadrature. For components A and F , the integration error alone amounts to 1 mJy because they blend with C or are poorly defined, and to 0.3 mJy for components B and E .

For illustration, we show in Figures 1-5 1.7 GHz and 2.3 GHz

Date	ν GHz	suppl. Antennas	Δt min	$\Delta\nu$ MHz	Phase-ref
1994-02-28	5.0	Eb/Y/On/Me/No	~ 10	56	n
1999-11-20	1.7, 5.0, 15	Y1/Eb,Y1/Eb,Y1	108, 144, 144	32	n
2000-03-06	1.7, 5.0, 15	Y1/Eb,Y1/Eb,Y1	108, 144, 136	32	n
2000-11-30	1.7, 5.0, 15	Y1/Eb,Y1/Eb,Y1	108, 144, 144	32	n
2002-09-22	1.7, 2.3, 5.0	Eb	114, 107, 112	64	y
2004-06-14	5.0, 22		199, 94	64	y
2004-11-03	5.0, 22		194, 82	64	y
2005-04-04	5.0, 22		195, 107	64	y
2005-08-18	5.0, 22		192, 107	64	y

Table 1. Summary of the observations. We give the observing dates, the frequencies observed, antennas supplementing the VLBA (Eb - Effelsberg, Y1 - one VLA antenna, Y - phased VLA, Me - Medicina, On - Onsala 85, No - Noto), the integration times, the bandwidths, and whether phase referencing was used or not. 2-bit sampling was used except 1994, when 1-bit sampling was used.

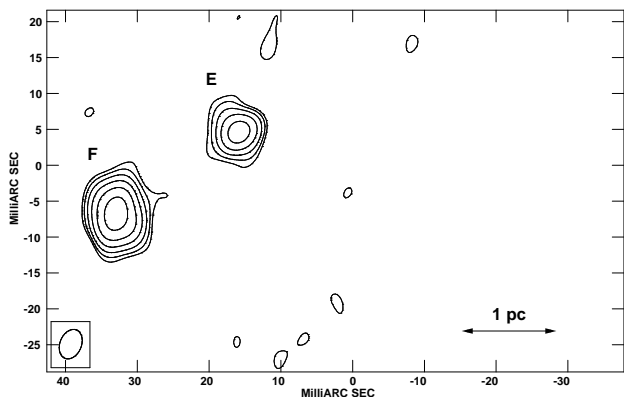


Figure 1. 1.7 GHz, phase-referenced and self-calibrated image of NGC 3079, observed on 22 September 2002. Axes are relative to RA 10h01m57.7906s Dec 55°40′47.1788″ (J2000), and self-calibration produced no measurable shift in the coordinates from phase referencing. Contours are drawn at $0.18 \text{ mJy beam}^{-1} \times 2^N$ ($N = 0, 1, 2, \dots$), and the beam size is $4.26 \times 2.99 \text{ mas}^2$. Only components *E* and *F* have been detected, and a wider region is shown to demonstrate that *A*, *B*, and *C* are not visible.

images from the 22 September 2002 epoch, 5 GHz and 22 GHz images from the 18 August 2005 epoch, and a 15 GHz image from the 30 November 2000 epoch. Details can be found in the image captions.

Caption to Table 2 Component and image parameters. Note that the 22 GHz flux densities are not reliable because self-calibration was marginal, see the discussion in Section 2.3.

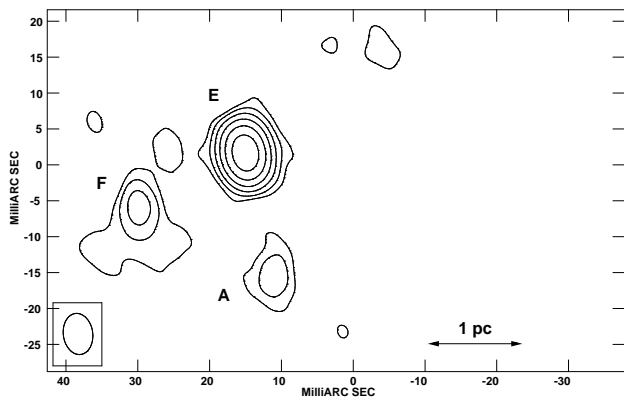


Figure 2. 2.3 GHz, phase-referenced and self-calibrated image of NGC 3079, observed on 22 September 2002. Axes are relative to RA 10h01m57.7906s Dec 55°40′47.1788″ (J2000), and self-calibration produced no measurable shift in the coordinates from phase referencing. Contours are at $0.39 \text{ mJy beam}^{-1} \times 2^N$ ($N = 0, 1, 2, \dots$), and the beam size is $5.75 \times 4.10 \text{ mas}^2$. Components *E* and *F* are weaker than at 1.7 GHz, and *A* is weak, but detected.

3 RESULTS

3.1 The maser emission

The purpose of observing the maser emission in this project was to phase reference the radio continuum emission to a quasi-stationary point (cf. the next section). In our data, the 1σ thermal noise per channel is 12 mJy beam^{-1} , only allowing us to detect the brightest features. We therefore do not attempt an astrophysical modelling of the maser emission. A spectrum showing all detected lines is shown in Figure 6.

3.2 Position of *B* with respect to the maser emission

One of the aims of the 22 GHz observations was to measure the positions of *A* and *B* with respect to the water maser emission. We found that the separation of the brightest maser feature at 956 km s^{-1} from the continuum component *B* was $6.7 \text{ mas} \pm 0.14 \text{ mas}$, with a position angle of 82° . This is in agreement with measurements by Trotter et al. (1998) ($6.7 \text{ mas} \pm 0.1 \text{ mas}$ in PA 81°), Sawada-Satoh et al. (2002) ($\approx 6.7 \text{ mas}$ in PA 81°), and Kondratko et al. (2005) ($6.74 \text{ mas} \pm 0.13 \text{ mas}$ in PA $80.75^\circ \pm 1.04^\circ$), which do not reveal any conclusive motion between Jan-

Date	Component parameters				Int. flux density				Image parameters			
	Peak flux density mJy beam ⁻¹				mJy				Image rms	b_{maj}	b_{min}	PA
	A	B	E	F	A	B	E	F	mJy beam ⁻¹	mas	mas	°
<i>Observations at 1.7 GHz</i>												
2002-09-22			4.2±0.2	9.7±0.5			5.4±0.6	15.3±1.3	0.06	5.1	3.5	-22
<i>Observations at 2.3 GHz</i>												
2002-09-22	1.2±0.1		19.8±1.0	2.1±0.2	1.9±1.0		21.0±1.2	7.2±0.7	0.13	6.0	4.3	12
<i>Observations at 5 GHz</i>												
1999-11-20	24.8±1.2	12.8±0.7	3.1±0.2		27.1±1.7	15.9±1.0	4.1±0.6		0.097	3.0	3.0	0.0
2000-03-06	23.3±1.2	13.1±0.7	3.1±0.2		26.0±1.6	18.7±1.1	3.2±0.6		0.095	3.0	3.0	0.0
2000-11-30	22.9±1.1	13.2±0.7	3.8±0.2		23.8±1.6	18.8±1.1	6.4±0.6		0.092	3.0	3.0	0.0
2002-09-22	21.1±1.1	14.0±0.7	5.4±0.3		26.0±1.6	22.4±1.3	7.9±0.7	6.9±1.1	0.089	3.0	3.0	0.0
2004-06-14	41.7±2.1	16.6±0.8	5.4±0.3		47.0±2.6	21.8±1.2	8.9±0.7		0.085	3.0	3.0	0.0
2004-11-03	41.7±2.1	15.8±0.8	5.3±0.3		47.5±2.6	21.2±1.2	7.9±0.7		0.084	3.0	3.0	0.0
2005-04-04	40.5±2.0	15.2±0.8	5.7±0.3		46.1±2.5	21.7±1.2	9.1±0.7		0.067	3.0	3.0	0.0
2005-08-18	42.8±2.1	14.6±0.7	5.6±0.3		50.1±2.7	21.1±1.2	9.2±0.7		0.080	3.0	3.0	0.0
<i>Observations at 15 GHz</i>												
1999-11-20	6.7 ±0.8	46.2±4.6			8.1 ±1.3	50.0±5.0			0.39	3.0	3.0	0.0
2000-03-06	7.6 ±0.9	53.6±5.4			9.5 ±1.5	55.4±5.6			0.46	3.0	3.0	0.0
2000-11-30	16.2±1.6	53.7±5.4			17.6±2.0	57.8±5.8			0.27	3.0	3.0	0.0
<i>Observations at 22 GHz</i>												
2004-11-03	(28.6)	(81.9)			(28.6)	(80.6)			0.99	3.0	3.0	0.0
2005-04-04	(49.0)	(70.1)			(54.1)	(69.8)			0.84	3.0	3.0	0.0
2005-08-18	(132.8)	(62.5)			(147.1)	(67.1)			2.09	3.0	3.0	0.0

Date	r(B-A) mas	PA(A) °	r(B-E) mas	PA(E) °
<i>Observations at 5 GHz</i>				
1994-02-28	24.03±0.42	126.6±1.0		
1999-11-20	26.22±0.21	126.3±0.5	26.26±0.21	86.7±0.5
2000-03-06	26.41±0.21	126.2±0.5	26.17±0.21	86.9±0.5
2000-11-30	26.53±0.21	126.6±0.5	25.91±0.21	87.4±0.5
2002-09-22	27.20±0.21	127.4±0.5	25.77±0.21	88.5±0.5
2004-06-14	27.77±0.21	126.9±0.5	25.89±0.21	88.7±0.5
2004-11-03	27.79±0.21	126.8±0.5	26.13±0.21	88.6±0.5
2005-04-04	27.69±0.21	126.8±0.5	25.79±0.21	87.9±0.5
2005-08-18	27.85±0.21	126.5±0.5	25.79±0.21	88.5±0.5
<i>Observations at 15 GHz</i>				
1999-11-20	26.82±0.21	128.0±0.5		
2000-03-06	26.76±0.21	127.5±0.5		
2000-11-30	26.77±0.21	127.2±0.5		
<i>Observations at 22 GHz</i>				
2004-11-03	28.24±0.14	127.0±0.3		
2005-04-04	28.39±0.14	127.2±0.3		
2005-08-18	28.50±0.14	126.8±0.3		

Table 3. Distances (r) and position angles (PA) of components A and E with respect to B.

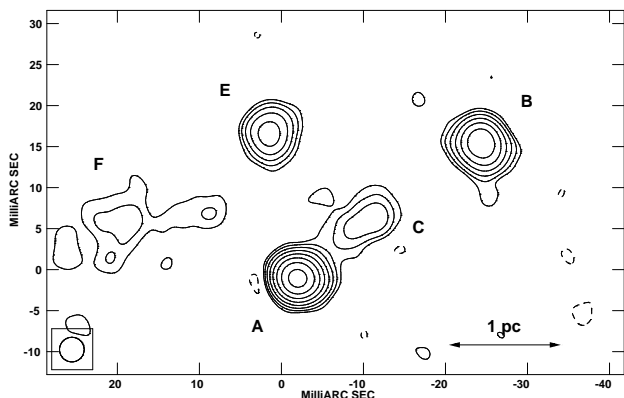


Figure 3. Example of a 5 GHz phase-referenced and self-calibrated image of NGC 3079, observed on 18 August 2005. At this frequency, all components can be seen. Components A, B, and E are still strong, the jet-like feature C between A and B is clearly detected, and F is resolved and faint, but detected. Axes are relative to RA 10h01m57.7906s Dec 55°40′47.1788″ (J2000), and self-calibration produced no measurable shift in the coordinates from phase referencing. Contours are drawn at $0.24 \text{ mJy beam}^{-1} \times 2^N$ ($N = 0, 1, 2, \dots$). The data have been tapered to a resolution of $3 \times 3 \text{ mas}^2$.

uary 1995 and March 2001. This means that component B has been stationary with respect to the maser emission for a decade. If the masers trace a molecular disk around the central massive black hole (Kondratko et al. 2005; Trotter et al. 1998), and their velocity dispersion is 400 km s^{-1} , or $0.0013 c$, then masers moving parallel to the plane of the sky could have moved by about 0.013 l.y. , or 0.004 pc in 10 yr. This corresponds to 0.06 mas , which would not have been noticed. Hence B can be regarded as stationary with respect to the central black hole powering the AGN, and measuring proper motions relative to B is therefore equivalent to measuring them relative to the black hole.

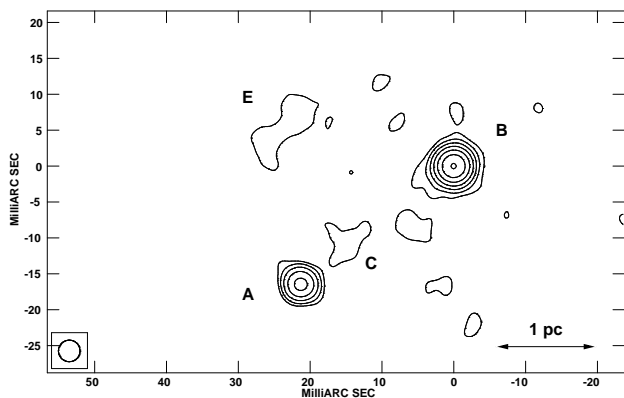


Figure 4. Example of a 15 GHz image of NGC 3079, observed on 30 November 2000. Components A and B are clearly detected, but there are only hints of components C and E. Absolute positions were not measured (phase referencing was not used), contours are at $0.81 \text{ mJy beam}^{-1} \times 2^N$ ($N = 0, 1, 2, \dots$). The data have been tapered to a resolution of $3 \times 3 \text{ mas}^2$.

3.3 Separation of A and B

VLBI observations of NGC 3079 have shown early on that the separation of A and B is increasing (Middelberg et al. 2005, Kondratko et al. 2005). We have plotted the previously published measurements of the separation of A and B in Fig. 7, together with our new measurements.

The pre-1998 data show a steady expansion of the source, with the notable exception of the 5 GHz measurement by Trotter et al. (1998). The data taken between 1999 and 2003 already indicate a slightly slower expansion rate, and the 2004-2005 5 GHz data clearly show that the expansion has come to a halt. We note that the separation of A and B is consistently larger at higher frequencies, and we therefore restrict our analysis of the proper motions to 5 GHz whenever possible.

The separations measured at higher frequencies do not follow the same trend as the 5 GHz measurements. The separations at

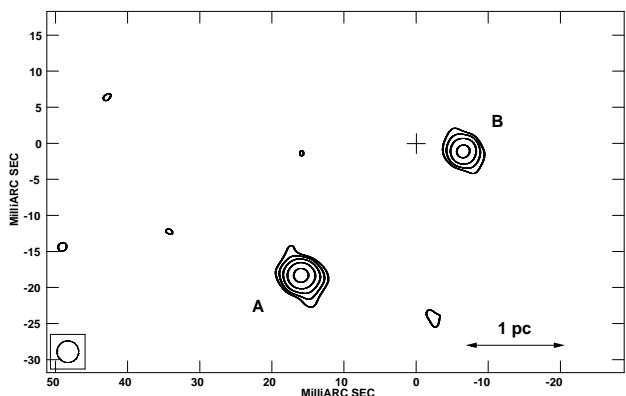


Figure 5. Example of a 22 GHz continuum image of NGC 3079, observed on 18 Aug 2005. Only components *A* and *B* have been detected, and then with relatively low SNR. Phase referencing to the brightest maser did not yield absolute positions at this frequency, contours are at $6.3 \text{ mJy beam}^{-1} \times 2^N$ ($N = 0, 1, 2, \dots$). The data have been tapered to a resolution of $3 \times 3 \text{ mas}^2$, which caused a large increase of the image noise. The cross indicates the position of the brightest maser feature.

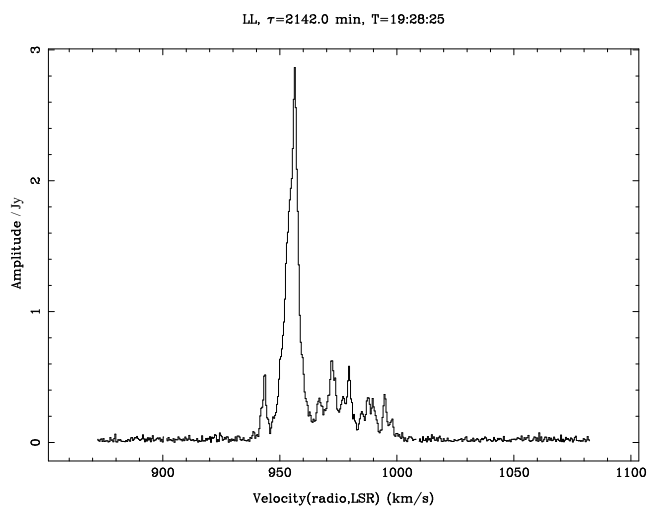


Figure 6. A spectrum of the water maser emission in NGC 3079, derived from averaging the cross-power spectra of all baselines. No lines were detected outside the velocity range shown.

both 15 GHz and 22 GHz are larger than that at 5 GHz; the 15 GHz data from 1999-2000 imply a larger separation and do not seem to confirm the expansion seen at 5 GHz; the 22 GHz data even seem to indicate that the expansion is continuing. However, this apparent disagreement on the evolution of the separation of *A* and *B* at low (5 GHz) and high (15 GHz and 22 GHz) frequencies can be explained as a consequence of optical depth effects causing a frequency-dependent core shift in either or both components. We postulate that at 5 GHz we see only an outer layer of the component(s) where the general kinematic properties of the whole actual emission region could be defined. At 15 GHz and 22 GHz, the optical depth of the ambient medium allows us to see predominantly into a denser emission region with slightly different kinematic properties.

We have fitted linear functions to all separations observed in 1985-1996, to our 5 GHz observations from 1999-2002, and to our 5 GHz observations from 2004-2005. The results are shown in Ta-

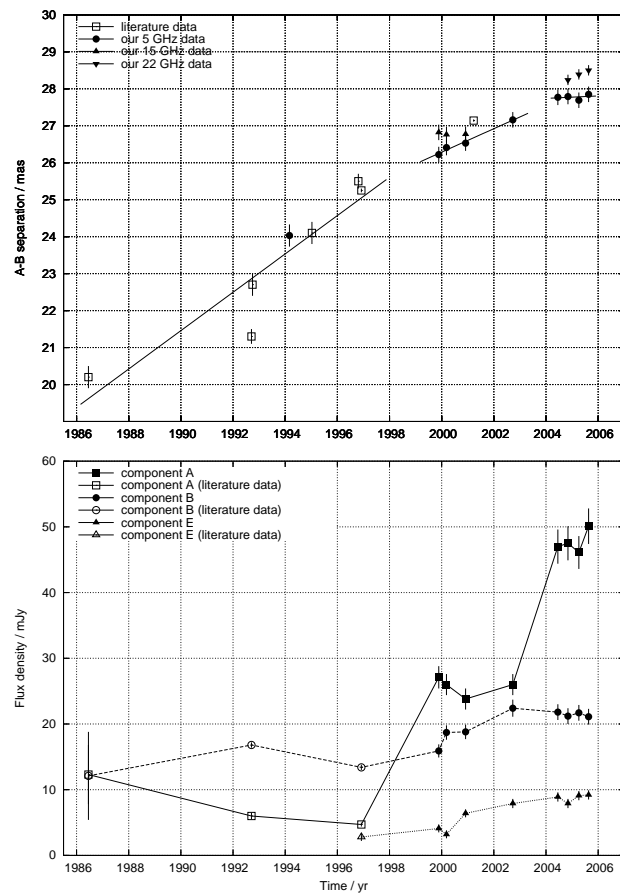


Figure 7. *Upper panel:* The evolution of the separation of *A* and *B*, using data from the literature and our measurements. Literature data are denoted with open symbols and have been taken from Irwin & Seaquist (1988) (epoch 1986.455, 5 GHz), Trotter et al. (1998) (epochs 1992.706, 5 GHz, and 1992.745, 8 GHz), Sawada-Satoh et al. (2000) (epoch 1996.802, 8 GHz), and Kondratko et al. (2005) (epochs 1996.919, 5 GHz, and 2001.225, 22 GHz) *Lower panel:* The 5 GHz flux densities of components *A*, *B*, and *E*. Only 5 GHz literature data, denoted with open symbols, were incorporated in this diagram and were taken from the same publications as for the panel above. Measurements of *A*, *B*, and *E* have been connected with solid, dashed, and dotted lines to help guide the eye.

Period	v_{ang} mas yr^{-1}	Δv_{ang} mas yr^{-1}	β	$\Delta\beta$
1985-1996	0.52	0.10	0.12	0.02
1999-2002	0.32	0.03	0.08	0.01
2004-2005	0.03	0.09	0.01	0.02

Table 4. Results of the linear fits to the separation of *A* with respect to *B* as a function of time. v_{ang} and Δv_{ang} are the apparent angular speed and its associated error, and β and $\Delta\beta$ are the corresponding values of $\beta = v/c$, assuming that the motion is in the plane of the sky at a distance of 15 Mpc.

ble 4 and are drawn as solid lines in Figure 7. We illustrate the motion on the sky of *A* and *E* with respect to *B* in Figure 8.

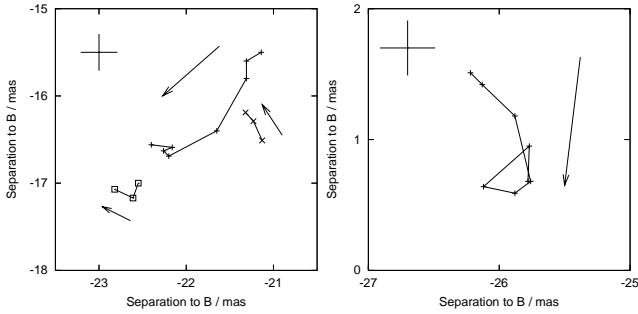


Figure 8. The motions of components *A* (left panel) and *E* (right panel) with respect to component *B*. Pluses represent measurements at 5 GHz, crosses those at 15 GHz, and squares those at 22 GHz. Arrows indicate the direction of motion of a component. The large crosses in the upper left corners indicate the errors of the measurements.

3.4 Motion of component *E*

Contrary to the separation of *A* and *B*, which appeared to increase steadily over more than a decade, the motion of *E* is more erratic. Its separation from component *B* is plotted in the right panel of Figure 8 and an arrow indicates the direction of motion. During our observations in 1999 and 2000, *E* appeared to be moving inwards, approximately in direction of the dynamical centre. This relatively clear trend stopped between November 2000 and our follow-up observations in September 2002. *E* has since described a figure resembling a circle, and in our latest measurements in August 2005 reached a point where it had been in November 2000.

3.5 Flux densities of *A*, *B*, and *E*

The evolution of the 5 GHz integrated flux densities of *A*, *B*, and *E* is shown in Fig. 7. The flux density of *A* exhibits two sudden increases, the first between the 1996 observations of Kondratko et al. (2005) and our observations in November 1999, and the other between our September 2002 and June 2004 observations. The mean of the pre-1999 flux densities of *A* is (7.7 ± 4.1) mJy, of our measurements between 1999 and 2002 is (26.0 ± 1.6) mJy, and of our post-2004 measurements is (48.5 ± 1.9) mJy. More importantly, these increases in flux density are coincident with the decelerations of component *A* as described in Section 3.3. The flux density of *B* shows no conclusive evolution over the years, whereas that of component *E* appears to be increasing slowly. The shape and internal structure of *E* evolved significantly over the years, and part of its erratic flux density evolution may be ascribed to this observation.

We note that in our last 5 GHz epoch, the brightness temperatures of *A*, *B*, and *E* were 39×10^7 K, 17×10^7 K, and 7×10^7 K, indicating that the emission is synchrotron emission from AGN or supernovae. Brightness temperatures of HII regions generally reach only of the order of 10^4 K (e.g., Condon et al. 1991), and are extended with sizes of $\gg 0.1''$ ($\gg 7.2$ pc in NGC 3079).

3.6 Spectral indices

We give in Table 5 all spectral indices calculated from the results in Table 2, ignoring the 22 GHz flux densities and using the convention that $S_\nu \propto \nu^\alpha$. Unfortunately, we do not have data at similar frequencies before and after the deceleration events seen in Figure 7, so we cannot analyse the spectral evolution of components during these events. Although our observations were designed to avoid resolution effects, we cannot rule out that the spectral index

of *F* is affected by its extent and by some of the 2.3 GHz flux density being missing due to the lack of short baselines.

4 DISCUSSION

We discuss the observational results as follows. In Section 4.1 we briefly comment on the spectral indices observed in NGC 3079; in Section 4.2 we show that components *A* and *B* are radio components in a jet which is undergoing interaction with the surrounding material; Section 4.3 demonstrates that the behaviour of *A* is unlikely to be due to jet bending and Doppler boosting; and Section 4.4 shows that components *E* and *F* are by-products of interactions of a jet with the surrounding material.

4.1 Spectral indices

During the epochs of 1999 and 2000, the spectral indices $\alpha_{15.4}^{5.0}$ of components *B* and *E* remained constant, and component *A* increased from -0.90 to -0.27 within the 8.5 months prior to the observations in November 2000.

The spectral indices measured simultaneously in September 2002 are more interesting. First, *A* has a strongly inverted spectrum with $\alpha_{5.0}^{2.3} = 3.37$, as has *E* with $\alpha_{2.3}^{1.7} = 4.49$. Second, *F* has a very steep spectrum between 1.7 GHz and 2.3 GHz, and there are several similar limits which also deserve explanation.

The inverted spectra of *A* and *E* in the September 2002 epoch can be modelled in terms of a free-free absorber in front of the components (similarly inverted spectra and limits can be explained using the same reasoning, but we lack the data for modelling). In the presence of a free-free absorber, the observed flux density, S_ν , of a component can be related to the intrinsic flux density at 1 GHz, S_0 , of the component by

$$S_\nu = S_0 \left(\frac{\nu}{\text{GHz}} \right)^{\alpha_0} \times \exp(-\tau_{ff}), \quad (1)$$

where α_0 is the intrinsic spectral index and τ_{ff} is the optical depth of the absorber with

$$\tau_{ff} = 0.0824 \left(\frac{T}{\text{K}} \right)^{-1.35} \left(\frac{\nu}{\text{GHz}} \right)^{-2.1} \int \frac{N_+}{\text{cm}^{-3}} \frac{N_-}{\text{cm}^{-3}} \frac{ds}{\text{pc}} \quad (2)$$

(Osterbrock 1989). The temperature, T , is commonly assumed to be 10^4 K, N_+ and N_- are the densities of positive and negative charges in the absorber (assumed to be equal), and ds is the path length along the line of sight. The integral is called the emission measure and is referred to as k hereafter. Equation 1 has three unknowns, the intrinsic flux density, S_0 , the intrinsic spectral index, α_0 , and the emission measure, k . It can be solved when the flux density has been measured at a minimum of three frequencies. When upper and lower limits are ignored, we can solve Equation 1 for *A*, *E*, and *F*, taking into account the measurements at 1.7 GHz, 2.3 GHz, 5.0 GHz, and 15.4 GHz. In the case of *A*, we use the simultaneous 2.3 GHz and 5.0 GHz measurements from 2002 and add the 15.4 GHz measurements from November 2000. Hence variability may affect the results. The models are plotted in Figure 9.

The spectrum of component *F* is concave and so is not described by a free-free absorbed power law, and we have instead fitted a simple power-law to the three spectral points. For component *A* we find $\alpha_0 = -1.01$, $S_0 = 305$ mJy, and $k = 7.4 \times 10^7$ pc cm $^{-6}$, leading to an optical depth at 5 GHz of 0.83. Thus *A* appears to be a rather normal source of synchrotron emission behind a moderately thick free-free absorber. In the case of

Epoch	SI	A	B	E	F
1999-11-20	$\alpha_{15.4}^{5.0}$	-1.07 ± 0.2	1.02 ± 0.15	$< -1.12 \pm 0.12$	-
2000-03-06	$\alpha_{15.4}^{5.0}$	-0.90 ± 0.2	0.97 ± 0.15	$< -0.75 \pm 0.15$	-
2000-11-30	$\alpha_{15.4}^{5.0}$	-0.27 ± 0.2	1.00 ± 0.15	$< -1.84 \pm 0.08$	-
2002-09-22	$\alpha_{2.3}^{1.7}$	$> 7.80 \pm 5.3$	-	4.49 ± 0.54	-2.49 ± 0.6
	$\alpha_{2.3}^{2.3}$	3.37 ± 0.57	$> 5.22 \pm 0.53$	-1.26 ± 0.19	-0.06 ± 0.34
	$\alpha_{5.0}^{1.7}$	$> 4.61 \pm 0.06$	$> 4.47 \pm 0.05$	0.35 ± 0.18	-0.74 ± 0.24

Table 5. Spectral indices of NGC 3079 components. Limits have been calculated using three times the image rms.

E, however, the intrinsic spectral index is $\alpha_0 = -4.40$, the intrinsic flux density is $S_0 = 17\,000$ mJy, and the emission measure is 5.3×10^7 pc cm $^{-6}$, leading to τ_{ff} at 5 GHz of 0.59. Again the properties of the absorber are reasonable, but α_0 is difficult to explain.

One possible interpretation is that the population of synchrotron electrons has been cut off from the central engine and has aged. The population will lose the high-energy electrons first, leading to a sharp drop in the observed spectral energy distribution towards higher frequencies. The steep spectral index of $\alpha_{2.3}^{1.7} = -2.49$ of *F* could also arise from such a situation, for which we argue in Section 4.4.

Another possibility is that the electron energy distribution is not a power-law, but is a relativistic thermal distribution. Such models have been considered by, e.g., Jones & Hardee (1979) and Beckert & Duschl (1997), and they usually reveal an exponential cutoff at high frequencies. Both explanations are unsatisfactory because they require the electron distribution cutoff to lie very close to the frequency at which $\tau_{ff} = 1$, but we can offer no better solution.

The result is robust against amplitude errors. Only when the measurements at 1.7 GHz and 5.0 GHz are increased by as much as 50 %, and the 2.3 GHz amplitude is decreased by 50 % does Equation 1 yield “common” values for α_0 of component *E*. Amplitude errors of this magnitude, and in the required sense, are unlikely.

Another possibility is resolution effects arising from the lack of short interferometer spacings and gaps in the (u, v) -coverage, both of which could lead to an underestimate of a partially resolved emission component. In particular in the case of *F* we cannot exclude that the flux is underestimated at 2.3 GHz or 5 GHz. In this case the spectral indices $\alpha_{2.3}^{1.9}$ and $\alpha_{5.0}^{2.3}$ given in Table 5 should be regarded as lower limits. For example, fitting a simple power-law spectrum for *F* to the three flux densities in Table 2 yields a spectral index of $\alpha = -0.78 \pm 0.29$, which is close to the canonical value of $\alpha = -0.7$.

4.2 A jet interacting with the external medium at the location of components *A* and *B*

That components *A* and *B* are jet features is strongly supported by the elongated structure between them (component *C*, Fig. 3, and component *D*, Fig. 3 in Trotter et al. 1998), by their high speed of separation before 2003, and because the line joining components *A* and *B* crosses the dynamical centre of the accretion disk in NGC 3079 (Kondratko et al. 2005). This position will be called the position of the central engine hereafter. The spectral properties of *A* and *B* lead Trotter et al. (1998) (see also Kondratko et al. 2005) to suggest that they are lower redshift and lower luminosity versions of compact symmetric objects, whose observational properties are known to be due to the interaction between jets and their

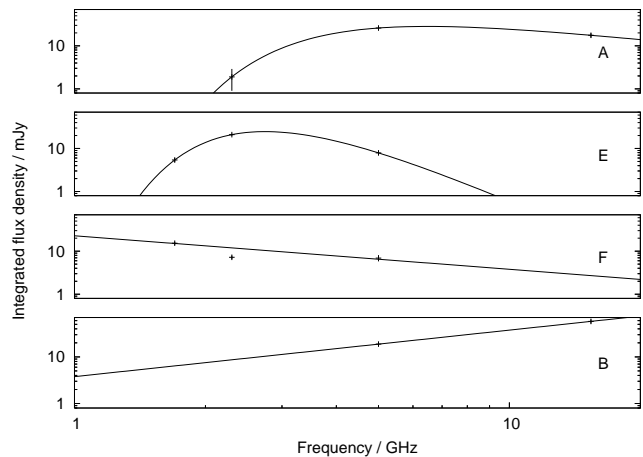


Figure 9. Spectra of components *A*, *E*, *F*, and *B*, measured in September 2002 and using 15 GHz data from November 2000. In the cases of components *A* and *E* the lines represent the model described in Section 4.1, whereas simple power-laws have been used for *B* and *F*.

high density external medium. These authors reported components *A* and *B* to have similar spectra, which correspond to synchrotron self-absorbed or free-free absorbed regions with turn-over frequencies in the range of 8 GHz to 10 GHz. Moreover, Middelberg et al. (2005) reported the spectra of the radio continuum components within the innermost 1 pc to 2 pc from the position of the central engine to be consistent with an scenario in which the nucleus of NGC 3079 is embedded in a dense medium. All these lines of evidence point to a jet-external medium interaction scenario.

Our new results show that component *B* has remained essentially stationary both in position and in flux density since 2000. In contrast, component *A* underwent two significant flux density increases with two corresponding decelerations, the last one completely halting the advance of this component.

Thus, these new results not only agree with the previously proposed jet-feature nature of components *A* and *B* interacting with the dense external medium, they also add further and stronger support to this scenario. The “brighter-when-slower” behaviour of component *A* is expected when a propagating jet encounters a progressively denser external medium region (e.g. a non-homogeneous dense cloud). The numerical simulations of Wang et al. (2000) and Saxton et al. (2005) are clear about what happens in that case. If the jet is “weak” (i.e. much less denser and/or much less energetic) with respect to the external dense cloud¹, the impact slows

¹ see Wang et al. (2000) for the definition of the parameters controlling the jet weakness with regard to its external cloud, and for examples of weak and powerful jets

down the advance of the “hot-spot” of the jet and raises its pressure. This pressure increase enhances the synchrotron emission. In the approximation of Saxton et al. (2001, 2002), an increase of the synchrotron emissivity² by a factor of 10, as experienced by component *A* between 1997 and 2005 (see Fig. 7), would occur if the pressure increased by a factor of ~ 3.5 .

4.3 Unlikely jet Doppler boosting scenario for component *A*

Note that there is still a scenario that has not been proposed before and that might, in principle, explain the “brighter-when-slower” behaviour of component *A*. This scenario also involves a jet but the reason for component *A*’s deceleration and brightening is the change of propagation direction of component *A* towards the line of sight, together with the Doppler boosting of the synchrotron radiation.

If the emission of component *A* is beamed relativistically then the observed flux density, S_ν , and the intrinsic flux density, S'_ν , are related by

$$S_\nu = \delta^3 S'_\nu, \quad (3)$$

where δ is the Doppler factor³ (e.g. Hughes & Miller 1991). An increase in the observed flux density of component *A* by a factor of two (as was observed between the end of 2002 and the beginning of 2004) would imply an increase of δ by a factor of $2^{1/3}$, which would also be the minimum required value of the Doppler factor after the beginning of 2004. As, by that time the condition $\theta \approx 0^\circ$ is required (because the motion of *A* in the plane of the sky has stopped), the intrinsic bulk plasma speed is constrained to be $\beta \gtrsim 0.23 c$. An angle of the jet to the line of sight of $\sim 90^\circ$ (i.e. the jets are in the plane of the sky) is usually assumed if the accretion disk of the system is almost edge-on, as in the case of NGC 3079. The large acceleration required both to bring the bulk plasma from $\beta \approx 0.13 c$ to $\beta \approx 0.23 c$ and to bend the jet beam by an amount of 45° or larger, make the jet-Doppler boosting scenario rather unlikely. A lower angle ($\gtrsim 45^\circ$) is assumed here to account for the fact that the jet is clearly not aligned with the angular momentum of the disk (see e.g. Kondratko et al. 2005) but at $\sim 45^\circ$ from such direction.

Hence, we conclude that the Doppler boosting scenario requires the jet in NGC 3079 at the location of *A* to bend by $\sim 45^\circ$ in a time range of only one year. In such conditions, a strong impact with the external medium unavoidably produces such extreme bending. In this case, the Doppler boosting scenario brings us again to the interaction of the jet with the external medium.

4.4 Components *E* and *F* as by-products of jet-external medium interaction

The fact that components *E* and *F* were found at positions not aligned with the jet between components *A* and *B* made Kondratko et al. (2005) suggest that *E* and *F* were intrinsically different from *A* and *B*. In addition, the spectral properties of *E* and *F* (with much steeper spectra than those corresponding to optically thin synchrotron spectra) led Kondratko et al. (2005) to pro-

pose that *E* and *F* are consistent with ageing synchrotron sources; i.e. with no injection of fresh non-thermal electrons.

Kondratko et al. (2005) showed that the possibility that *E* and *F* are radio supernovae is highly unlikely. Instead, they proposed two different scenarios to explain the properties of *E* and *F*: *a*) either they are remains of emission from a wobbling jet which was ejected earlier in orientations different from the current jet direction or *b*) they are shocks in a wide-angle, pc-scale outflow interacting with its external medium. Within the latter picture, the outflow would be a pc-scaled version of the kpc-scale bipolar super-bubbles observed in radio continuum emission (Duric & Seaquist 1988; Baan & Irwin 1995; Irwin & Saikia 2003), in [N II]+H α emission (Veilleux et al. 1994; Cecil et al. 2001) and in soft X-ray continuum emission (Cecil et al. 2002).

We consider the jet wobbling scenario (*a*) very unlikely since no evidence has been found to support a systematic change of the position angle of the current jet. In this scenario, the jet axis defined as the line which connects components *A* and *B*, should systematically change with time, which has not been observed between 1994 and 2005 (cf. Table 3). Furthermore, component *C* nicely lines up with the *A*-*B* axis in all images since Irwin & Seaquist (1988) observed NGC 3079 for the first time with VLBI. Hence, during this time range, the jet wobbling scenario can be safely ruled out.

Although scenario (*b*) is not as unlikely as the jet wobbling scenario, we still find it difficult to imagine an outflow ejected from the central engine in NGC 3079 which interacts with the dense external medium and produces a shock moving *inwards*, in the opposite sense to the assumed *outflow*, as detected for component *E* in 1999-2000 (Figure 8).

Here, we propose an alternative scenario to account for the presence of synchrotron emission regions from non-thermal aging electrons close to the pc-scale jets in NGC 3079. This new scenario comes up naturally from the jet/dense-external-medium interaction picture previously proposed to explain the behaviour of component *A*. Our idea is based on the two-dimensional numerical simulations of jets in inhomogeneous media reported by Saxton et al. (2005)⁴.

Their grid of simulations, on which a tenuous medium is also populated by a relatively small filling factor of dense clouds, show that when the filling factor of the clouds is large, the jet has more possibilities to be disrupted and to form channels through which the shocked radio emitting plasma can flow between the clouds. The formation of a hierarchical structure of nested lobes (not always producing strong radio emission) and an outer enclosing bubble seems unavoidable in all the simulated conditions. Having in mind this scenario, it is difficult not to find a close, at least qualitative, relation between our component *A* with the region of the simulated jet in which the first dense cloud is encountered and the jet is disrupted; and between components *E* and *F* with the simulated lobes or knots of already shocked material. In the simulations, this material slowly flows from the first shocked region along the opened channels between the clouds (see e.g. Fig. 11 of Saxton et al. 2005) and not necessarily outwards, away from the central engine, because their motions depend on the cloud-obstacles that they encounter in propagation. This could explain why component *E* does not move outwards but inwards, towards the central engine (Figure 8). The simulations of Saxton et al. (2005) show that the lobes of shocked material can be found at large distances (relative to the

² $j_\nu \propto p^{(3-\alpha)/2}$, where p is the pressure and α is the spectral index of the synchrotron emission. We assume $\alpha \approx -0.7$ here.

³ $\delta = [\Gamma(1 - \beta \cos \theta)]^{-1}$ where $\Gamma = (1 - \beta^2)^{-1/2}$ is the Lorentz factor, β is the speed in units of c and θ is the angle between the direction of the flow and the line of sight.

⁴ The scaling of the results from Saxton et al. (2005) was set to apply their quantitative results to kpc-scale jets. However, for us who use their study on a qualitative way only, their results are equally applicable.

jet size) from the first shocked region and in directions that are far from where the original straight jet would have propagated.

A consequence of this is that, as the clouds move, plasma channels that initially emit synchrotron emission can eventually be closed, cutting off synchrotron-emitting regions from a fresh supply of non-thermal particles. As a consequence, the electron population of synchrotron-emitting regions is expected to age. This process manifests itself in an overall decrease of flux density and the steepening of radio spectra, as high-energy particles lose their energy more quickly and radio emission at higher frequencies decreases first. In NGC 3079, the 5 GHz flux density of component *E* has approximately doubled between 1999 and 2005, which seems to disagree with the scenario of an aging electron population. However, we note that *E* underwent significant internal evolution in 1999 and 2000. This evolution may be caused by compression of the component, which caused the observed increase in flux density.

5 SUMMARY AND CONCLUSIONS

Based on the similarities of the spectra of GPS sources with those of components *A* and *B*, previous studies proposed these components to be regions in which a jet, launched from the central super-massive engine in NGC 3079, interacts with the dense external medium. Moreover, Middelberg et al. (2005) reported the spectra of the radio continuum components within the innermost 1 pc to 2 pc from the accretion disk to be consistent with an scenario in which the nucleus of NGC 3079 is embedded in a dense medium. We have shown that the structure and the time evolution of the radio continuum emission in the innermost pc around the accretion disk in NGC 3079 behaves as expected for a jet interacting with a clumpy external medium. Hence, our new results not only agree with both the jet scenario and the jet-interaction scenario previously proposed, but also strongly support both of them.

Within our proposed scenario, depending on the properties of the cloudy medium in which they are embedded, *A* and *B* are expected to continue separating from the dynamic centre of the accretion disk once they are able to drill through the cloud that stopped them, as was proposed for the expanding phase of the jet in III Zw 2 (Brunthaler et al. 2005). Note however, that the re-activation of the expansion of components *A* and *B* might start to be significant after large time periods (depending on the relative properties of the jets and the clumpy medium on which they are embedded). Thus, these expansions may not be observable for years or tens of years. The spectra of components *E* and *F* should show evidence of a slowly ageing non-thermal electron population until they have faded completely. Although not required, they can be expected to move with speeds smaller than those previously measured for *A* and in directions which do not necessarily have to point outwards from the central engine in NGC 3079.

The simulations of Saxton et al. (2005) show that, if the filling factor of dense clouds in the surrounding medium of the jet is high, the momentum of the jet spreads at the first strong interaction and forms a slowly expanding bubble which grows larger than the jet itself, which indicates that the jet is impeded from propagating freely. If one assumes a large filling factor of dense clouds surrounding the central region of NGC 3079, the interaction scenario offers, as a natural consequence of the slower propagation of the jet, the explanation for the origin of the kpc-scale bipolar super-bubbles observed in radio continuum emission, [N II]+H α emission and soft X-ray continuum emission in NGC 3079.

There is at present little doubt about the presence of strong

interactions of the radio plasma with the inter-stellar medium in Seyfert galaxies (Oosterloo et al. 2000). As for NGC 3079, evidence for interaction of the jets with their external medium in subgalactic-scales seems to be common in Seyfert galaxies (e.g. NGC 1068 and NGC 4151, Wilson & Ulvestad 1982; III Zw 2, Brunthaler et al. 2005). Hence, it appears reasonable to apply the interaction scenario to the whole class of Seyfert galaxies. This would give a satisfactory explanation for why in a large fraction of Seyfert galaxies large-scale bipolar super-bubbles are observed (e.g. Colbert et al. 1996, Colbert et al. 1996) instead of well collimated, kpc-scale jets as in radio-loud AGN.

ACKNOWLEDGMENTS

I. Agudo acknowledges financial support from the EU Commission for Science and Research through the ENIGMA network (contract HPRN-CT-2002-00321). The VLBA is an instrument of the National Radio Astronomy Observatory, which is a facility of the National Science Foundation of the U.S.A. operated under cooperative agreement by Associated Universities, Inc. (U.S.A.). We thank M. Perucho for reviewing the manuscript.

REFERENCES

- Baan W. A., Irwin J. A., 1995, *ApJ*, 446, 602
- Beckert T., Duschl W. J., 1997, *A&A*, 328, 95
- Brunthaler A., Falcke H., Bower G. C., Aller M. F., Aller H. D., Teräsranta H., 2005, *A&A*, 435, 497
- Cecil G., Bland-Hawthorn J., Veilleux S., 2002, *ApJ*, 576, 745
- Cecil G., Bland-Hawthorn J., Veilleux S., Filippenko A. V., 2001, *ApJ*, 555, 338
- Colbert E. J. M., Baum S. A., Gallimore J. F., O’Dea C. P., Christensen J. A., 1996, *ApJ*, 467, 551
- Colbert E. J. M., Baum S. A., Gallimore J. F., O’Dea C. P., Lehnert M. D., Tsvetanov Z. I., Mulchaey J. S., Caganoff S., 1996, *ApJS*, 105, 75
- Condon J. J., Huang Z.-P., Yin Q. F., Thuan T. X., 1991, *ApJ*, 378, 65
- de Vaucouleurs G., de Vaucouleurs A., Corwin H. G., Buta R. J., Paturel G., Fouque P., 1991, *Third Reference Catalogue of Bright Galaxies*. Springer-Verlag Berlin Heidelberg New York
- Duric N., Seaquist E. R., 1988, *ApJ*, 326, 574
- Haschick A. D., Baan W. A., 1985, *Nature*, 314, 144
- Haschick A. D., Baan W. A., Schneps M. H., Reid M. J., Moran J. M., Guesten R., 1990, *ApJ*, 356, 149
- Heckman T. M., 1980, *A&A*, 87, 152
- Hughes P. A., Miller L., 1991, *Introduction: synchrotron and inverse-Compton radiation. Beams and Jets in Astrophysics*, p. 1
- Irwin J. A., Saikia D. J., 2003, *MNRAS*, 346, 977
- Irwin J. A., Seaquist E. R., 1988, *ApJ*, 335, 658
- Jones T. W., Hardee P. E., 1979, *ApJ*, 228, 268
- Kondratko P. T., Greenhill L. J., Moran J. M., 2005, *ApJ*, 618, 618
- Middelberg E., 2004, *PhD thesis*, University of Bonn
- Middelberg E., Krichbaum T. P., Roy A. L., Witzel A., Zensus J. A., 2005, in Romney J., Reid M., eds, *ASP Conf. Ser. 340: Future Directions in High Resolution Astronomy Approaching NGC 3079 with VLBI*, p. 140
- Middelberg E., Roy A. L., Nagar N. M., Krichbaum T. P., Norris R. P., Wilson A. S., Falcke H., Colbert E. J. M., Witzel A., Fricke K. J., 2004, *A&A*, 417, 925

- Miyoshi M., Moran J., Herrnstein J., Greenhill L., Nakai N., Diamond P., Inoue M., 1995, *Nature*, 373, 127
- Mundell C. G., Wrobel J. M., Pedlar A., Gallimore J. F., 2003, *ApJ*, 583, 192
- Oosterloo T. A., Morganti R., Tzioumis A., Reynolds J., King E., McCulloch P., Tsvetanov Z., 2000, *AJ*, 119, 2085
- Osterbrock D. E., 1989, *Astrophysics of Gaseous Nebulae and Active Galactic Nuclei*. University Science Books
- Roy A. L., Colbert E. J. M., Wilson A. S., Ulvestad J. S., 1998, *ApJ*, 504, 147
- Sawada-Satoh S., Inoue M., Shibata K. M., Kamenno S., Migenes V., Nakai N., Diamond P. J., 2000, *PASJ*, 52, 421
- Sawada-Satoh S., Inoue M., Shibata K. M., Kamenno S., Nakai N., Migenes V., Diamond P. J., 2002, in Migenes V., Reid M. J., eds, *IAU Symposium 206: Cosmic Masers: From Proto-Stars to Black Holes* Proper motion of nuclear jet relative to a maser feature in NGC 3079. *Astronomical Society of the Pacific*, p. 404
- Saxton C. J., Bicknell G. V., Sutherland R. S., Midgley S., 2005, *MNRAS*, 359, 781
- Saxton C. J., Sutherland R. S., Bicknell G. V., 2001, *ApJ*, 563, 103
- Saxton C. J., Sutherland R. S., Bicknell G. V., Blanchet G. F., Wagner S. J., 2002, *A&A*, 393, 765
- Sosa-Brito R. M., Tacconi-Garman L. E., Lehnert M. D., Gallimore J. F., 2001, *ApJS*, 136, 61
- Trotter A. S., Greenhill L. J., Moran J. M., Reid M. J., Irwin J. A., Lo K., 1998, *ApJ*, 495, 740
- Veilleux S., Cecil G., Bland-Hawthorn J., Tully R. B., Filippenko A. V., Sargent W. L. W., 1994, *ApJ*, 433, 48
- Walker R. C., Dhawan V., Brisken W., Benson J., Kogan L., Romney J., 2005, Technical report, VLBA Test Memo 69: Inappropriate EOP on the VLBA Correlator. http://www.vlba.nrao.edu/memos/test/test69memo/eop_problem.html
- Wang Z., Wiita P. J., Hooda J. S., 2000, *ApJ*, 534, 201
- Wilson A. S., Ulvestad J. S., 1982, *ApJ*, 263, 576